RESPONSE OF A REACTING CRYOGENIC OXYGEN JET TO TRANSVERSE ACOUSTIC FORCING

Justin S. Hardi[(1)], Samuel C. L. Webster [(1)], and Michael Oschwald[(1)]

[(1)] Institute of Space Propulsion, German Aerospace Center (DLR), Lampoldshausen, Germany

KEYWORDS: liquid propellant rocket engine, cryogenic propellants, combustion instability, optical diagnostics

ABSTRACT:

The intact length of the liquid oxygen core of a shear coaxial rocket flame has been measured for varying amplitude of transverse acoustic excitation. The experiment was performed using an experimental rocket combustor with five shear-coaxial injection elements running liquid oxygen and hydrogen for a range of injection conditions. The first transverse acoustic mode of the rectangular combustion chamber is excited and the response of the dense oxygen core is measured from shadowgraph imaging. Improvements in the imaging technique and post-processing method allowed reliable automated processing of far larger data sets compared to previous work. These data sets describe the amplitude dependent reduction in intact core length.

1. INTRODUCTION

High frequency (HF) combustion instability can occur in liquid propellant rocket engines when acoustic oscillations and unsteady energy release from combustion become coupled. While generally considered to have good stability characteristics, engines using the propellant combination liquid oxygen/hydrogen (LOx/H_2) with shear coaxial injectors are not immune to the problem [1–3].

In shear coaxial type injectors a central jet of cryogenic LOx, the ‘core’, is surrounded by a faster annulus of gaseous fuel. The behaviour of the LOx core after injection is thought to be important to the coupling of acoustic disturbances with combustion [4, 5]. For example, the distance it penetrates into the combustion chamber before breaking up, called the intact core length, influences the distribution of energy release in the combustion chamber, and may even be a source of unsteady heat release [6].

Numerous experimental investigations of intact core length, as well as spray character and breakup behaviour, can be found in literature [7–10]. Backlit shadowgraph photography is a common diagnostic for such studies. An important observation from the literature is the discrepancy between core length measurements under cold-flow and hot-fire conditions [11]. Correlations derived from cold-flow experiments systematically underestimate intact core length, highlighting the importance of measurements under industrially representative, hot-fire conditions [12, 13].

The response of the LOx core to high amplitude acoustic oscillations is relevant to the understanding of HF combustion instabilities. Instabilities of transverse acoustic modes, with acoustic gas motions perpendicular to the direction of injection, are the kind of most concern to industrial engines [3].

Experiments striving to observe the LOx core under representative operating conditions often use siren excitation of the combustion chamber to force transverse-mode acoustic resonance [14–18]. Shadowgraph imaging from such experiments shows that the intact core shortens in length due to accelerated breakup and mixing driven by the transverse acoustic gas oscillations [14, 15, 19]. Previous work by the authors established a trend of decreasing core length in relation to acoustic amplitude [14]. Core length was measured from series of shadowgraph images taken during varying acoustic forcing amplitude.

By virtue of the high frame rate of the imaging, a change in the dominant breakup behaviour of the LOx core could also be observed. Simultaneous OH* emission imaging showed corresponding change in the extent, emission intensity, and dynamics of the flame [20]. This significant change in LOx core and flame

character has also been captured in numerical modelling of a LOx/methane rocket flame [21]. The model was then used to address the heat release dynamics which are of importance to coupling with the acoustic field.

While such numerical modelling, and the previous experimental work in [14, 15, 19] provided valuable qualitative insight, and measurements of LOx core response were presented in [14], the data sets describing core response are limited. More complete data sets would allow the results to be broadly applied in low-order stability models or in validation of high-fidelity numerical simulation.

The present work aims to address this need by extending the database of intact LOx core length measurements in [14]. The experimental combustor used for the measurements, designated 'BKH', can reproduce industrially relevant conditions. BKH operates at pressures from 40 to 60 bar, covering the sub- and supercritical regimes for oxygen. It has multiple shear coaxial injection elements with injection parameters representative of upper-stage, LOx/H_2 engines. Acoustic forcing achieves transverse mode acoustic pressure amplitudes up to 9% of mean chamber pressure (18% peak-to-peak), which is representative of dangerous, naturally occurring instabilities.

The BKH experiment was run for a broader range of operating conditions than achieved previously. High-speed shadowgraph imaging was again used as the primary diagnostic technique. The intact core length is measured with an automated core-recognition routine and compared to the forced acoustic amplitude for several tests with different operating conditions. Preliminary comparison is made between results from different operating conditions.

2. EXPERIMENTAL TECHNIQUE

Testing was conducted using the BKH experimental rocket combustor at the European Research and Technology Test Facility P8 for cryogenic rocket engines at DLR Lampoldshausen. BKH has a rectangular cross-section in order to fix the acoustic resonance frequencies and structures, and a secondary nozzle in the upper wall. The exhaust flow through the secondary nozzle is modulated with a toothed siren, or 'exciter', wheel to excite acoustic resonances inside the combustion chamber. Fig. 1 illustrates the main

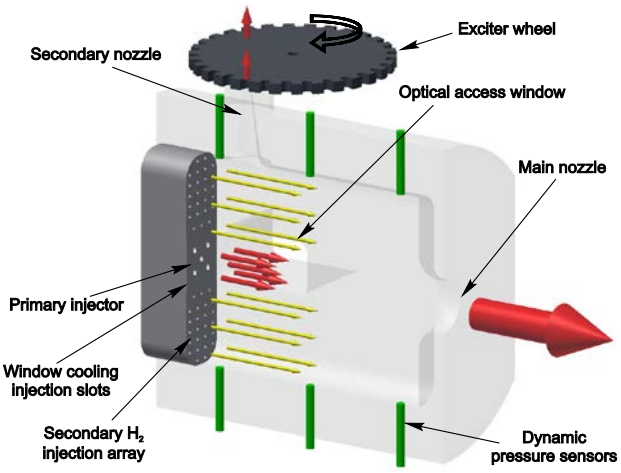

Figure 1. Conceptual illustration of the experimental combustor, BKH

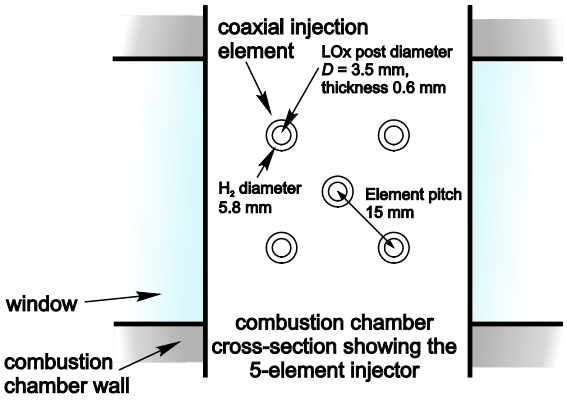

Figure 2. BKH injector dimensions

features of BKH. Optical access is provided to the near-injector region. Piezoelectric type dynamic pressure sensors are flush mounted along the upper and lower chamber walls. For further details on all aspects of the BKH system, the reader is directed to [22].

Injection of LOx/H_2 occurs through five shear coaxial injection elements with dimensions typical of those found in industrial upper stage engines. Element outlet dimensions are indicated in Fig. 2. Internal dimensions of the injection system can be found in [22]. The elements are arranged in a 'matrix' pattern, with one central element surrounded by the remaining four, evenly spaced. This arrangement of multiple elements was selected in order to create an environment for the central jet which resembles that of an element in an industrial engine, surrounded on all sides by other elements. The interaction of neighbouring flames is representative of the tightly packed arrangement found in industrial engines.

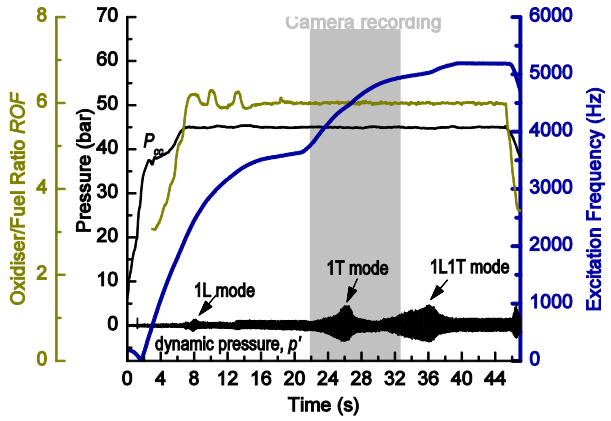

Figure 3. Test sequence

Table 1. Operating conditions.

Parameter		Range
Combustion chamber pressure	P_{CC}, bar	40 – 60
Primary injector mixture ratio	*ROF*	6
Per-element total mass flow rate	$\dot{m}$, g/s	66 – 130
Oxygen injection temperature	T_O, K	115 – 130
Oxygen injection velocity	u_O, m/s	6 – 12
Hydrogen injection temperature	T_H, K	60 – 310
Injection velocity ratio	*VR*	7 – 55
Momentum flux ratio	*J*	1.3 – 9.9

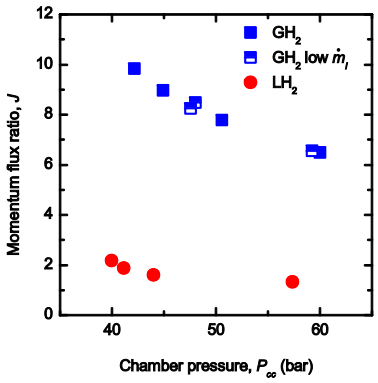

Figure 4. Operating conditions by momentum flux ratio

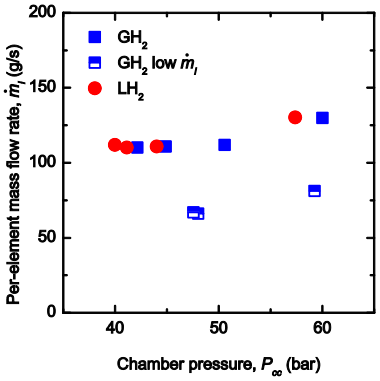

Figure 5 Operating conditions by primary per-element mass flow rate

Secondary H_2 is injected around the cluster of primary elements for cooling and flow conditioning purposes.

A typical test sequence is illustrated in Fig. 3, showing the temporal profile of combustion chamber pressure (P_{cc}), mixture ratio (*ROF*), acoustic excitation frequency, and dynamic pressure in the chamber (p'). The combustor is run to a steady state operating condition defined by P_{cc} and *ROF* and the excitation frequency is ramped up over a desired range. When the excitation frequency passes through the first transverse (1T) mode of the chamber, the high speed camera is triggered to record.

In this work, imaging results are examined from several tests with P_{cc} ranging from 40 to 60 bar and using hydrogen at either cryogenic or ambient temperature (T_H). The range of operating conditions and injection parameters for the tests are summarised in Table 1. Injection parameters are also plotted against P_{cc}, with Fig. 4 showing the range of H_2-to-LOx momentum flux ratio (*J*), and Fig. 5 showing per-element total mass flow rate ($\dot{m}_I$) for the primary elements. Tests with ambient T_H are referred to as 'GH_2', and with cryogenic T_H as 'LH_2'. In Fig. 5, some GH_2 tests have lower $\dot{m}$ of around 70 to 80 g/s. These tests are intended to provide lower oxygen injection velocities (u_O) to investigate the impact of this parameter on intact core length.

Acoustic excitation is achieved with the siren. The frequency of excitation is determined by controlling the rotational speed of the exciter wheel. In this test, the exciter wheel rotation was not driven by a servomotor, rather by the exhaust flow of the secondary nozzle itself. Rotation could be resisted with a purging nitrogen flow onto the wheel. Under these driving and resistive forces, the rotational speed of the wheel increases during a test, resulting in the profile of excitation frequency seen in Fig. 3. The first transverse (1T) resonance mode of the combustion chamber volume is excited as the excitation frequency passes through approximately 4200 Hz.

The acoustic field structure for the 1T mode can be reconstructed from p' measurements taken along the upper and lower chamber walls.

The pressure and velocity distributions for peak 1T amplitude, reconstructed through interpolating between p' sensor locations, are shown in Fig. 6. The 1T mode has a pressure node aligned approximately with main (horizontal) axis of the chamber. This means that exciting this mode subjects the spray flames to high amplitudes of oscillating acoustic gas motion, transverse to the direction of injection.

Observation windows in the walls of BKH provide optical access to the near injector region with a viewing area measuring 50 mm high and 100 mm long, with one side aligned with the injection plane and a height sufficient to view the entire 5-element injector. The setup of high-speed cameras is illustrated schematically in Fig. 7. Continuous backlighting for shadowgraph imaging is provided by a green LED source. Backlit shadowgraph images are recorded with a Photron Fastcam SA5 using blue-green and yellow filters for a wavelength pass-band tightly isolating the LED wavelength.

The recording duration of the camera is indicated on the test profile in Fig. 3. A recording rate of 6000 frames per second (fps), shutter speed 11 µs, and pixel resolution 1024 × 352, were used. These camera settings result in a spatial resolution of 0.11 mm per pixel. The injection velocity of LOx (u_O) is around 10 m/s, resulting in a flow displacement of less than one pixel (~ 0.1 mm) during exposure time. This means the images are sharp and suffer from little blurring.

An example of an instantaneous shadowgraph image is shown in Fig. 8. With injection from the left, the central and two nearest LOx cores are visible as dark jets in the image. The boundaries of the dense LOx core are well defined by their contrast with the bright background.

The optical setup and camera settings used here differ from previous BKH campaigns, resulting in image quality improvements for the benefit of the subsequent analysis. The most significant difference is the change in backlighting source from a Xenon lamp to a LED. The higher intensity backlight outshines more combustion emission and overcomes more absorption in the surrounding flow field, improving contrast between LOx core and background. Furthermore it allows shorter

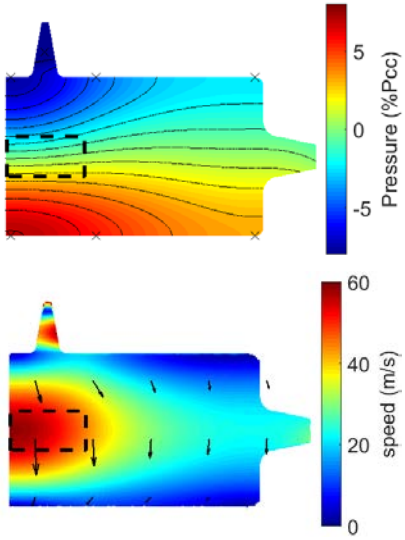

Figure 6. Acoustic pressure (above) and velocity distributions (below) reconstructed from dynamic pressure measurements during peak-amplitude excitation of the first transverse (1T) mode

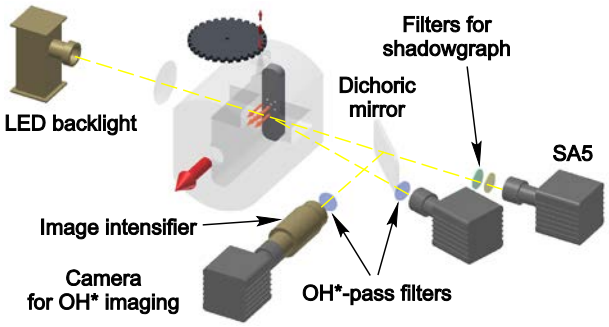

Figure 7. Optical setup

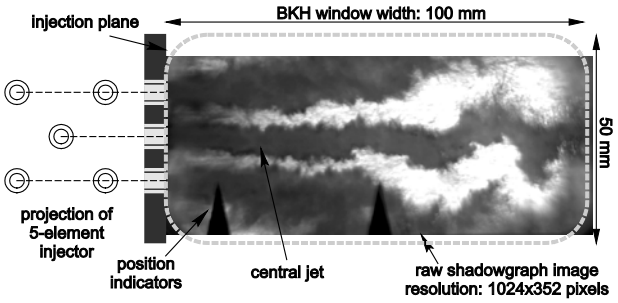

Figure 8. Example instantaneous shadowgraph image

exposure time, reducing motion-related blurring. These features improve the potential for automatic core recognition with standard image processing algorithms.

A lower framerate of 6000 fps was used here, compared to 20,000 fps in past campaigns. While the higher frame rate previously allowed direct temporal resolution of the LOx core response to acoustics, the lower frame rate

here allowed longer recording durations for better coverage of the range of excitation amplitudes over the course of ramped excitation.

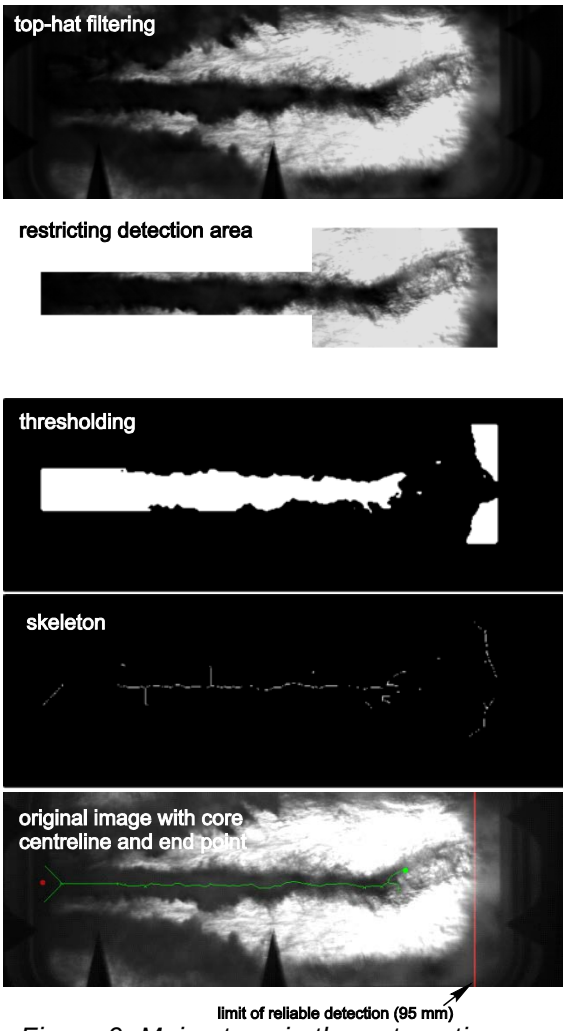

Figure 9. Main steps in the automatic core detection routine

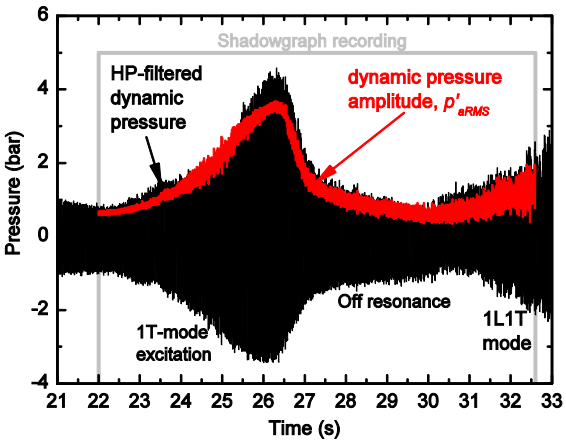

Figure 10. RMS-derived dynamic pressure amplitude

3. DATA PROCESSING METHODOLOGY

3.1. Image processing and core recognition

An automated routine was developed to measure the length of the intact central core from the shadowgraph images. The routine is based on a past attempt to automate BKH shadowgraph analysis, which suffered from poor reliability due to low image contrast.

The routine processes the images in the following steps, illustrated by example in Fig. 9. The boundary between the LOx core and the surrounding combustion products is highlighted by applying a top-hat filter. The use of a disc-shaped structuring element reduces the uneven texturing of turbulent flow/flame structures. The region surrounding the central core is selected by the user, to contain the scope of the area of detection. Then the core is clearly defined by converting to a binary image (black and white) based on an established grey level threshold. The core appears now as a white structure. A morphological operation fills the coherent white shape of the core with a skeleton and deletes detached structures to isolate the intact part of the core. The furthermost point of the skeleton is obtained and used to calculate the intact core length.

The backlighting was often refracted near the end of the optical access window, resulting in a dark area poorly contrasted from the dense LOx structures passing in front of it. The end of the field of accurate core detection is marked with a red line in the example in Fig. 9, and measurements exceeding this length were discarded. After limiting the allowed region of detection, an entire set of 63538 frames is processed with a reliability of 96%.

3.2. Data reduction

For each image and core-length measurement, a corresponding value of acoustic amplitude is required. The trigger output signal from the high-speed camera allows the imaging to be synchronised with the test timeline. Values of acoustic pressure amplitude were obtained from a dynamic pressure sensor located in the lower chamber wall near the injection plane.

The raw signal, p', is first high-pass filtered with a cut-off frequency of 3200 Hz, since only the excited acoustic content is of interest. Then, a sliding RMS is calculated on the time vector corresponding to the instances of image

capture at 6000 fps. The RMS values are finally multiplied by the square root of 2, resulting in an envelope of acoustic pressure amplitude, herein referred to as RMS-derived pressure amplitude, p'_{aRMS}. The calculated p'_{aRMS} signal is overlaid on the raw p' signal in Fig. 10.

4. RESULTS AND DISCUSSION

4.1. Temporal response of core

First, the temporal response of the intact core length is examined. Zooming in on short samples of length 500 frames in Fig. 11, the temporal behaviour of core length is compared for three different acoustic amplitudes. The samples from off-resonance conditions with low relative amplitude (p'_{aRMS}/P_{cc}) of 3.2% and 4.1% still exhibit natural core breakup behaviour. Their saw-tooth profiles seen in Fig. 11 correctly reflect the growth and detachment mechanism of natural core breakup [12, 13, 22]. By comparison, the decrease in saw-tooth character of the sample for 6.9% amplitude reflects the change to an atomisation mechanism driven by transverse acoustic velocity, as described in previous work [14, 22].

A decrease in mean core length with increasing acoustic amplitude is also evident in Fig. 11. The course of core length over the entire imaging duration is plotted in Fig. 12, along with the p'_{aRMS} signal. Mean core length appears to follow the mirrored temporal profile of p'_{aRMS}, as excitation amplitude increases to around 8% of P_{cc} before decreasing back to off-resonance values.

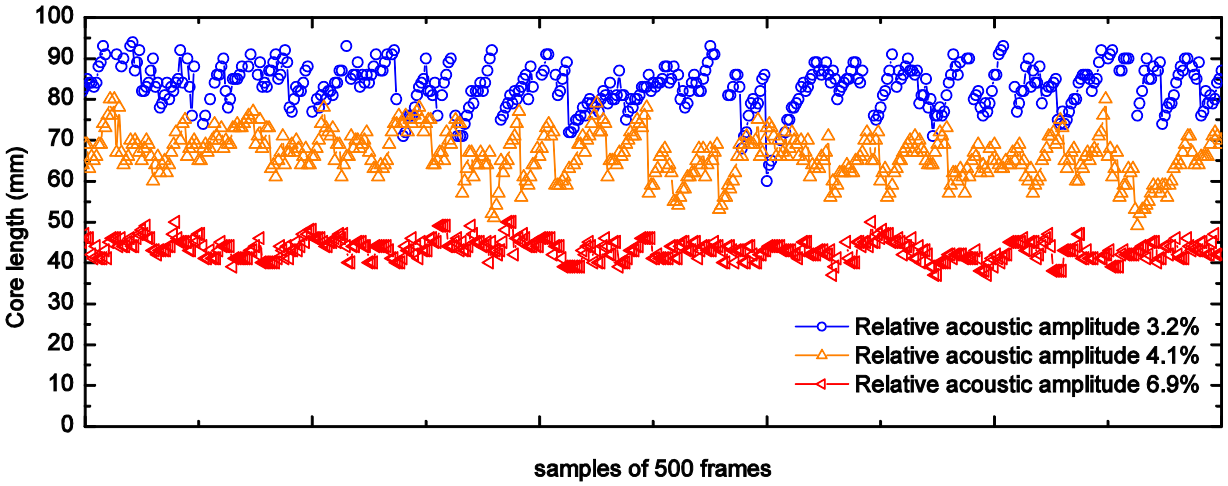

Figure 11. Temporal response of intact core length to various excitation amplitudes

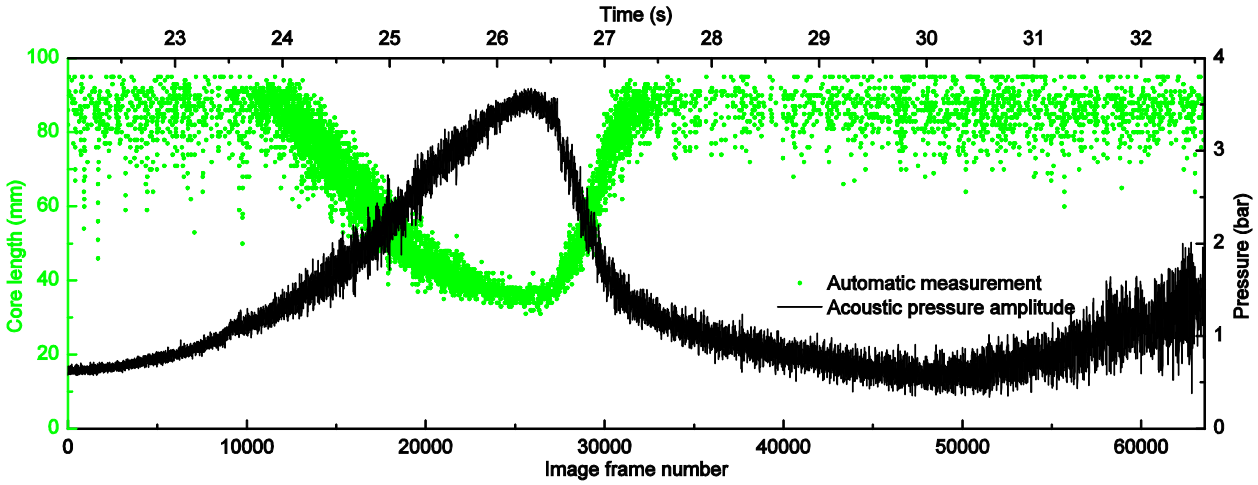

Figure 12. Temporal response of intact core length over course of recording duration

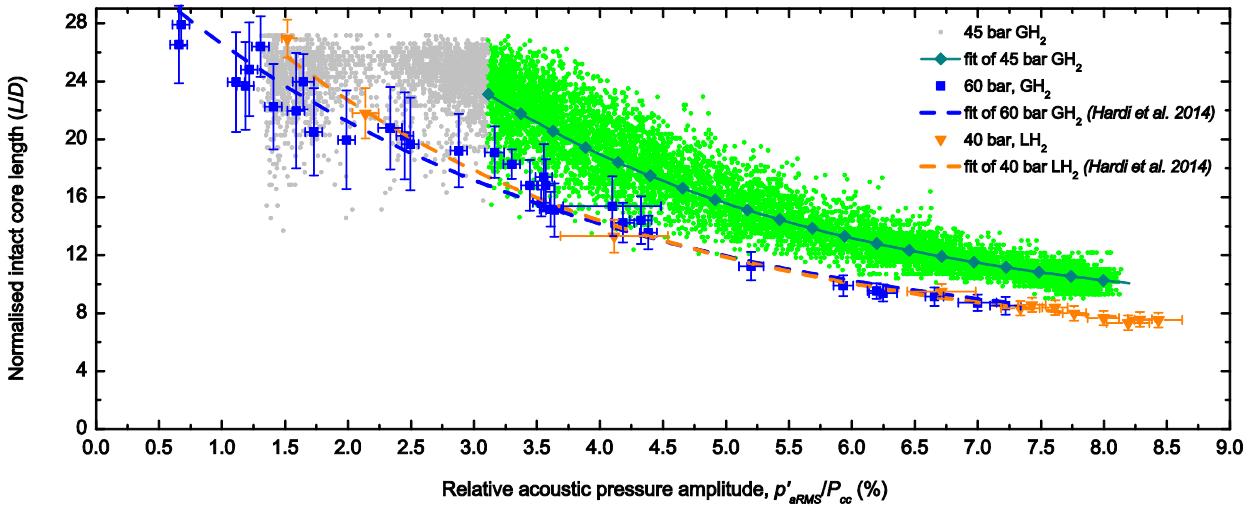

Figure 13. Amplitude response of intact core length (45 bar, GH_2) with fit curve, overlaid on previous results of Hardi et al. 2014 [14], *also with fit curves.*

The decrease in core length with increasing amplitude is accompanied by decreasing spread in measured core length. This decrease in core length fluctuation reflects the transition in atomisation breakup mechanism, also consistent with previous work [14, 22].

4.2. Amplitude response of core

The response of automatically measured core length with respect to acoustic amplitude for a 45 bar, GH_2 test is presented in Fig. 13. Core length is normalised with oxygen injector diameter, and p'_{aRMS} is normalised with P_{cc}. The automated measurements are overlaid on the manual core length measurements for 60 bar, GH_2 and 40 bar, LH_2 conditions published previously by Hardi et al. 2014 [14] for comparison.

The reduction in L/D with increasing p'_{aRMS}/P_{cc} appears to follow the trend in the previous data well, including a bend to shallower decline with increasing amplitude. The variance in L/D also decreases with increasing amplitude. From past work it is known that this is due to the dominant breakup behaviour of the LOx core transitioning from its natural growth-and-detachment mechanism to the transverse acoustic mechanism.

The mean L/D appears to be systematically longer in the new data set. Which test parameter is responsible for this offset is yet to be clarified.

The number density of measurements over the amplitude range is vastly increased by the automated routine. This will improve the statistical strength of the results compared to previous results, which were manually measured from shorter samples of imaging.

Nonlinear regression was used to fit curves to the data sets in Fig. 13. An asymptotic expression of the form $y = a - bc^x$ was found to describe well the portion of measurements corresponding to decreasing intact core length under increasing pressure amplitude. In this expression, Parameter a represents the minimum core length approached for very high acoustic amplitude. Parameter b determines the steepness of the curve, and together with parameter a defines the ordinate crossing $(a - b)$. Parameter c determines the acuteness of the curve, and could be interpreted as an indication of the susceptibility of the LOx core to the acoustic perturbation.

Where the end of the core was not entirely within the range of reliable detection, the data was excluded from the regression, in this case indicated by the greyed measurement points in Fig. 13. This means the fit describes only the core response from atomisation dominated by the transverse shedding mechanism driven by the acoustic field. Before this point, the natural shedding mechanism dominates and determines the mean intact core length. Therefore the ordinate crossing of the fit curve $(a - b)$ is not a measure of mean unperturbed core length.

A weighting was applied in the regression to improve the fit quality for higher p'_{aRMS}/P_{cc} values. As the amplitude increases and the acoustically driven atomisation mechanism

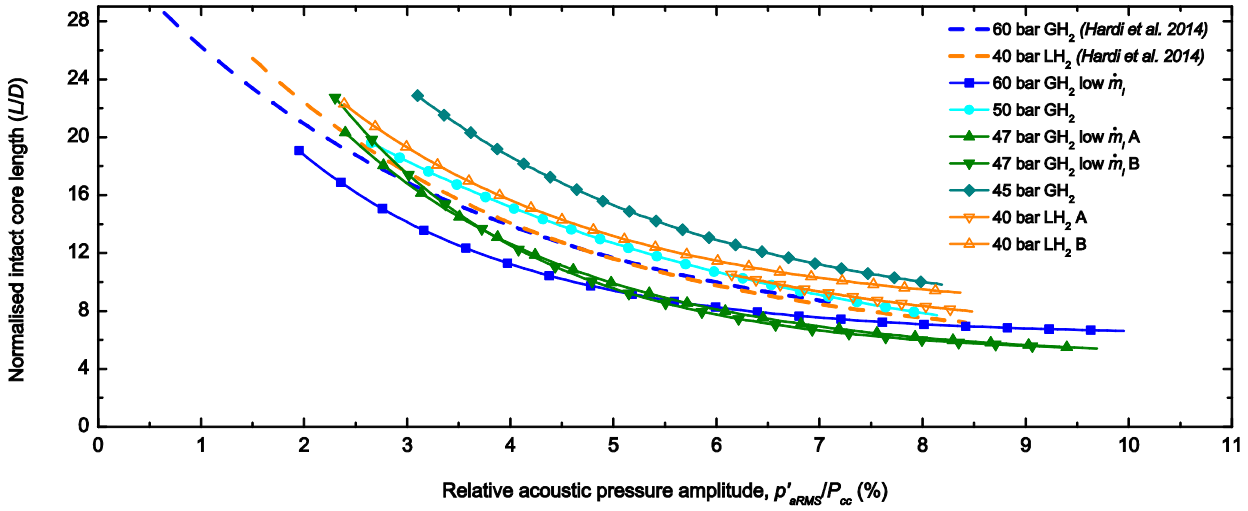

Figure 14. Amplitude response fit curves for all tests

dominates, the variance in core length measurements also decreases. It was therefore deemed important for the fit to describe the high amplitude end of the curve particularly well. Weighting proportional to $1/y^3$ achieved this goal.

The same data model with the same regression weighting fit was applied to all data sets processed with the core detection routine. The fit quality was high, with adjusted R^2 values generally above 0.88, with the exception of the two 40 bar, LH_2, low $\dot{m}_l$ tests for which the data set was smaller and had higher variance.

All fit curves are presented in Fig. 14, without extrapolation beyond the bounds of the subset of data used for the regression. Note that the two curves from Hardi et al. 2014 extend to lower amplitudes because manual measurements extended the entire length of the optical access window. The three curves representing the tests with low $\dot{m}_l$ are conspicuous in their acuteness. They appear to describe a LOx core more susceptible to acoustic perturbation, decreasing in length more quickly and approaching their converged lengths for lower amplitudes than in the other cases.

This preliminary comparison of LOx core response curves shows promise in revealing parameters governing the response. It remains to seek correlation of fit parameters to establish specific dependencies on injection and operating conditions.

5. CONCLUSION AND OUTLOOK

Past measurements of intact oxygen core length were extended with data from a new campaign. The current results build on previous work with a stronger statistical basis and wider range of operating conditions, with the aim of providing a data set more accessible for validation of computational models of injection-acoustic interaction.

The temporal and amplitude response of the core were consistent with past results. Core breakup behaviour was recovered correctly, and the core length decreased significantly with acoustic amplitude.

Nonlinear regression was used to fit trend lines to the portion of data representing retraction of the core under acoustic forcing. The fit was of high quality and allowed all data sets to be overlaid and compared.

The overlaid fit curves indicate clear dependence of the susceptibility of intact core length to transverse acoustic amplitude on injector mass flow rate. Future work will explore the dependence of core response on injection parameters in more detail and seek to collapse the data sets further.

ACKNOWLEDGMENTS

The authors wish to thank Dmitry Suslov, Alex Grebe, Hideto Kawashima, and the crew of the P8 test bench for their efforts in test operations. Thanks to Bernhard Knapp, Robert Stützer, and Silke Anders for setup and operation of optical diagnostics. Thanks to Scott Beinke for his assistance in data analysis.

REFERENCES

1. Preclik, D., Spagna, P. (1989). Low frequency and high frequency combustion oscillation phenomena inside a rocket combustion chamber fed by liquid or gaseous propellants. In: AGARD Conference Proceedings. NATO Advisory Group for Aeronautical Research and Development, Neuilly Sur Seine, France.
2. Harrje, D.T., Reardon, F.H. eds. (1972). Liquid propellant rocket combustion instability. NASA SP-194, Washington, DC.
3. Yang, V., Anderson, W.E. eds. (1995). Liquid rocket engine combustion instability. AIAA, Washington, DC.
4. Davis, D.W., Chehroudi, B. (2007). Measurements in an acoustically driven coaxial jet under sub-, near-, and supercritical conditions. *J. of Propulsion and Power*. **23**(2), pp364–374.
5. Davis, D.W., Chehroudi, B. (2006). Shear-coaxial jets from a rocket-like injector in a transverse acoustic field at high pressures. 44th AIAA Aerospace Sciences Meeting & Exhibit. AIAA, Reno, Nevada.
6. Mayer, W., Tamura, H. (1996). Propellant injection in a liquid oxygen/gaseous hydrogen rocket engine. Journal of Propulsion and Power. **12**(6), pp1137–1147.
7. Chigier, N., Reitz, R.D. (1995). Regimes of jet breakup and breakup mechanisms. In: Kuo, K. (ed.) Recent advances in spray combustion: spray atomization and droplet burning phenomena. pp109–136. AIAA, New York.
8. Farago, Z., Chigier, N. (1992). Morphological classification of disintegration of round jets in a coaxial airstream. *Atomization and Sprays*. **2** pp137–153.
9. Lasheras, J., Hopfinger, E. (2000). Liquid jet instability and atomization in a coaxial gas stream. *Annual Review of Fluid Mechanics*, pp275–308.
10. Miesse, C.C. (1955). The effect of ambient pressure oscillations on the disintegration and dispersion of a liquid jet. *J. of the American Rocket Society*. **25**(10), pp525–530,534.
11. Woodward, R.D. (1993). Primary atomization of liquid jets issuing from rocket engine coaxial injectors. PhD Thesis. Pennsylvania State University.
12. Locke, J.M., Pal, S., Woodward, R.D., Santoro, R.J. (2010). High speed visualization of LOX/GH2 rocket injector flowfield: hot-fire and cold-flow experiments. 46th AIAA/ASME/SAE/ASEE Joint Propulsion Conference & Exhibit. AIAA, Nashville, Tennessee.
13. Yang, B., Cuoco, F., Oschwald, M. (2007). Atomization and Flames in LOX/H2- and LOx/CH4- Spray Combustion. *Journal of Propulsion and Power*. **23**(4), pp763–771.
14. Hardi, J.S., Gomez Martinez, H.C., Oschwald, M., Dally, B.B. (2014). LOx jet atomization under transverse acoustic oscillations. *Journal of Propulsion and Power*. **30**(2), pp337–349.
15. Méry, Y., Hakim, L., Scouflaire, P., Vingert, L., Ducruix, S., Candel, S. (2013). Experimental Investigation of Cryogenic Flame Dynamics Under Transverse Acoustic Oscillations. *Comptes Rendus Mécanique*. **341**(1),–(2), pp100–109.
16. Rey, C., Ducruix, S., Richecoeur, F., Scouflaire, P., Candel, S. (2004). High Frequency Combustion Instabilities Associated with Collective Interactions in Liquid Propulsion. In: 40th AIAA/ASME/SAE/ASEE Joint Propulsion Conference & Exhibit. AIAA, Fort Lauderdale, FL.
17. Richecoeur, F., Ducruix, S., Scouflaire, P., Candel, S. (2008). Experimental investigation of high-frequency combustion instabilities in liquid rocket engine. *Acta Astronautica*. **62**(1), pp18–27.
18. Sliphorst, M., Knapp, B., Groening, S., Oschwald, M. (2012). Combustion Instability-Coupling Mechanisms Between Liquid Oxygen/Methane Spray Flames and Acoustics. *J. of Propulsion and Power*. **28**(6), pp1339–1350.
19. Richecoeur, F. (2006). Expérimentations et simulations numériques des interactions entre modes acoustiques transverses et flammes cryotechniques. PhD Thesis. École Centrale Paris.
20. Hardi, J., Beinke, S.K., Oschwald, M., Dally, B.B. (2014). Coupling of cryogenic oxygen-hydrogen flames to longitudinal and transverse acoustic instabilites. *J. of Propulsion and Power*. **30**(4), pp991–1004.
21. Hakim, L., Schmitt, T., Ducruix, S., Candel, S. (2015). Dynamics of a transcritical coaxial flame under a high-frequency transverse acoustic forcing: Influence of the modulation frequency on the flame response. *Combustion and Flame*. **162** pp3482–3502.
22. Hardi, J.S. (2012). Experimental investigation of high frequency combustion instability in cryogenic oxygen-hydrogen rocket engines. PhD Thesis. The University of Adelaide, Adelaide, Australia.